

The enhanced X-ray Timing and Polarimetry mission— eXTP for launch in 2030

Shuang-Nan Zhang^{1,2*}, Andrea Santangelo^{3,1,30}, Yupeng Xu¹, Hua Feng¹, Fangjun Lu¹, Yong Chen¹, Mingyu Ge¹, Kirpal Nandra⁴, Xin Wu⁵, Marco Feroci^{6,7}, Margarita Hernanz^{8,9}, Congzhan Liu¹, Huilin He¹, Yusa Wang¹, Weichun Jiang¹, Weiwei Cui¹, Yanji Yang¹, Juan Wang¹, Wei Li¹, Hong Li¹, Yuanyuan Du¹, Xiaohua Liu¹, Bin Meng¹, Xiangyang Wen¹, Aimei Zhang¹, Jia Ma¹, Maoshun Li¹, Gang Li¹, Liqiang Qi¹, Jianchao Sun¹, Tao Luo¹, Hongwei Liu¹, Xiaojing Liu¹, Fan Zhang¹, Laidan Luo¹, Yuxuan Zhu¹, Zijian Zhao¹, Liang Sun¹, Xiongtao Yang¹, Qiong Wu¹, Jiechen Jiang¹, Haoli Shi¹, Jiangtao Liu¹, Yanbing Xu¹, Sheng Yang¹, Laiyu Zhang¹, Dawei Han¹, Na Gao¹, Jia Huo¹, Ziliang Zhang¹, Hao Wang¹, Xiaofan Zhao¹, Shuo Wang¹, Zhenjie Li¹⁰, Ziyu Bao¹⁰, Yaoguang Liu¹⁰, Ke Wang¹¹, Na Wang¹¹, Bo Wang¹², Langping Wang¹³, Dianlong Wang¹⁴, Fei Ding¹², Lizhi Sheng¹⁵, Pengfei Qiang¹⁵, Yongqing Yan¹⁵, Yongan Liu¹⁵, Zhenyu Wu¹⁶, Yichen Liu¹⁶, Hao Chen¹⁶, Yacong Zhang¹⁷, Hongbang Liu¹⁸, Alexander Altmann⁴, Thomas Bechteler⁴, Vadim Burwitz⁴, Carlo Fiorini⁴, Peter Friedrich⁴, Norbert Meidinger⁴, Rafael Strecker⁴, Luca Baldini^{19,23}, Ronaldo Bellazzini¹⁹, Raffaella Bonino^{20,23}, Andrea Frassà^{20,23}, Luca Latronico²⁰, Simone Maldera²⁰, Alberto Manfreda²¹, Massimo Minuti¹⁹, Melissa Pesce-Rollins¹⁹, Carmelo Sgrò¹⁹, Stefano Tugliani^{20,23}, Giovanni Pareschi²⁴, Stefano Basso²⁴, Giorgia Sironi²⁴, Daniele Spiga²⁴, Gianpiero Tagliaferri²⁴, Andrii Tykhonov⁵, Stéphane Paltani²⁵, Enrico Bozzo²⁵, Christoph Tenzer³, Jörg Bayer³, Youli Tuo³, Honghui Liu³, Yonghe Zhang²⁶, Zhiming Cai²⁶, Huaqiu Liu²⁶, Wen Chen²⁶, Chunhong Wang²⁶, Tao He²⁶, Yehai Chen²⁶, Chengbo Qiu²⁶, Ye Zhang²⁶, Jianchao Feng²⁶, Xiaofei Zhu²⁶, Heng Zhou²⁶, Shijie Zheng¹, Liming Song¹, Haoli Shi¹, Jinzhou Wang¹, Shumei Jia¹, Zewen Jiang¹, Xiaobo Li¹, Haisheng Zhao¹, Ju Guan¹, Juan Zhang¹, Chengkui Li¹, Yue Huang¹, Jinyuan Liao¹, Yuan You¹, Hongmei Zhang^{27,28}, Wenshuai Wang^{27,28}, Shuang Wang^{27,28}, Ge Ou^{27,28}, Hao Hu^{27,28}, Jingyan Shi^{27,28}, Tao Cui^{27,28}, Xiaowei Jiang^{27,28}, Yaodong Cheng^{27,28}, Haibo Li^{27,28}, Yanjun Xu¹, Silvia Zane²⁹, Cosimo Bambi^{30,31}, Qingcui Bu³², Simone Dall’Osso³³, Alessandra De Rosa³⁴, Lijun Gou³⁵, Sebastien Guillot³⁶, Long Ji^{37,38}, Ang Li³⁹, Jirong Mao⁴⁰, Alessandro Patruno⁴¹, Giulia Stratta⁴², Roberto Taverna⁴³, Sergey Tsygankov⁴⁴, Phil Uttley⁴⁵, Anna L. Watts⁴⁵,

*Corresponding author (email: zhangsn@ihep.ac.cn)

Xuefeng Wu⁴⁶, Renxin Xu^{47,48}, Shuxu Yi¹, Guobao Zhang⁴⁰, Liang Zhang¹,
Wen Zhao⁴⁹, and Ping Zhou⁵⁰

- ¹State Key Laboratory for Particle Astrophysics, Institute of High Energy Physics, Beijing 100049, China
²University of Chinese Academy of Sciences, Beijing 100049, China
³Institut für Astronomie und Astrophysik, Eberhard Karls Universität, Tübingen 72076, Germany
⁴Max Planck Institute for Extraterrestrial Physics, Garching 85748, Germany
⁵Department of Nuclear and Particle Physics, University of Geneva, Geneva CH-1211, Switzerland
⁶INAF—Istituto di Astrofisica e Planetologia Spaziali, Rome I-00133, Italy
⁷INFN—Roma Tor Vergata, Rome I-00133, Italy
⁸Institute of Space Sciences (ICE, CSIC), Cerdanyola del Vallès 08193, Spain
⁹Institut d'Estudis Espacials de Catalunya(IEEC), Barcelona 08034, Spain
¹⁰High Energy Photon Source, Institute of High Energy Physics, Beijing 100049, China
¹¹Experimental Physics Division, Institute of High Energy Physics, Beijing 100049, China
¹²Center for Precision Engineering, Harbin Institute of Technology, Harbin 150001, China
¹³State Key Laboratory of Advanced Welding and Joining, Harbin Institute of Technology, Harbin 150006, China
¹⁴School of Chemistry and Chemical Engineering, Harbin Institute of Technology, Harbin 150001, China
¹⁵State Key Laboratory of Transient Optics and Photonics,
Xi'an Institute of Optics and Precision Mechanics, Chinese Academy of Sciences, Xi'an 710119, China
¹⁶State Key Laboratory of Transducer Technology, Shanghai Institute of Microsystem and Information Technology,
Chinese Academy of Sciences, Shanghai 200050, China
¹⁷National Key Laboratory of Science and Technology on Micro/Nano Fabrication, School of Integrated Circuits, and
the Beijing Advanced Innovation Center for Integrated Circuits, Peking University, Beijing 100871, China
¹⁸Guangxi Key Laboratory for Relativistic Astrophysics, School of Physical Science and Technology,
Guangxi University, Nanning 530004, China
¹⁹Istituto Nazionale di Fisica Nucleare, sezione di Pisa, Pisa I-56127, Italy
²⁰Istituto Nazionale di Fisica Nucleare, sezione di Torino, Torino I-10125, Italy
²¹Istituto Nazionale di Fisica Nucleare, sezione di Napoli, Napoli I-80126, Italy
²²Dipartimento di Fisica, Università di Pisa, Pisa I-56127, Italy
²³Dipartimento di Fisica, Università degli Studi di Torino, Torino I-10125, Italy
²⁴Osservatorio Astronomico di Brera, Istituto Nazionale di Astrofisica, Milano 20121, Italy
²⁵Department of Astronomy, University of Geneva, Versoix 1290, Switzerland
²⁶Innovation Academy for Microsatellites of CAS, Shanghai 201203, China
²⁷Computing Center, Institute of High Energy Physics, Beijing 100049, China
²⁸National High Energy Physics Science Data Center, Institute of High Energy Physics, Beijing 100049, China
²⁹Mullard Space Science Laboratory, University College London, Dorking RH5 6NT, UK
³⁰Center for Astronomy and Astrophysics, Center for Field Theory and Particle Physics, and
Department of Physics, Fudan University, Shanghai 200438, China
³¹School of Natural Sciences and Humanities, New Uzbekistan University, Tashkent 100007, Uzbekistan
³²Institute of Astrophysics, Central China Normal University, Wuhan 430079, China
³³INAF—Istituto di Radioastronomia, Bologna I-40129, Italy
³⁴INAF—Istituto di Astrofisica e Planetologie Spaziali, Rome 00133, Italy
³⁵National Astronomical Observatories, Chinese Academy of Sciences, Beijing 100012, China
³⁶Institut de Recherche en Astrophysique et Planétologie, Centre National de la Recherche Scientifique, Toulouse F-31028, France
³⁷School of Physics and Astronomy, Sun Yat-sen University, Zhuhai 519082, China
³⁸CSST Science Center for the Guangdong-Hong Kong-Macao Greater Bay Area, Zhuhai 519082, China
³⁹Department of Astronomy, Xiamen University, Xiamen 361005, China
⁴⁰Yunnan Observatory, Chinese Academy of Sciences, Kunming 650011, China
⁴¹Institute of Space Sciences (ICE, CSIC), Campus UAB, Barcelona 08193, Spain
⁴²INAF, Osservatorio di Astrofisica e Scienza dello Spazio, Bologna I-40129, Italy
⁴³Department of Physics and Astronomy, University of Padova, Padova I35131, Italy
⁴⁴Department of Physics and Astronomy, University of Turku, Turku 20014, Finland
⁴⁵Anton Pannekoek Institute for Astronomy, University of Amsterdam, Amsterdam 1098 XH, the Netherlands
⁴⁶Purple Mountain Observatory, Chinese Academy of Sciences, Nanjing 210023, China
⁴⁷Department of Astronomy, School of Physics, Peking University, Beijing 100871, China
⁴⁸Kavli Institute for Astronomy and Astrophysics, Peking University, Beijing 100871, China
⁴⁹Department of Astronomy, University of Science and Technology of China, Hefei 230026, China
⁵⁰School of Astronomy and Space Science, Nanjing University, Nanjing 210023, China

Received June 4, 2025; accepted August 22, 2025; published online September 24, 2025

In this paper, we present the current status of the enhanced X-ray Timing and Polarimetry mission, which has been fully approved for launch in 2030. eXTP is a space science mission designed to study fundamental physics under extreme conditions of matter density, gravity, and magnetism. The mission aims at determining the equation of state of matter at supra-nuclear density,

measuring the effects of quantum electro-dynamics, and understanding the dynamics of matter in strong-field gravity. In addition to investigating fundamental physics, the eXTP mission is poised to become a leading observatory for time-domain and multi-messenger astronomy in the 2030s, as well as providing observations of unprecedented quality on a variety of galactic and extragalactic objects. After briefly introducing the history and a summary of the scientific objectives of the eXTP mission, this paper presents a comprehensive overview of: (1) the cutting-edge technology, technical specifications, and anticipated performance of the mission's scientific instruments; (2) the full mission profile, encompassing spacecraft design, operational capabilities, and ground segment infrastructure.

X-ray instrumentation, X-ray polarimetry, X-ray timing, space mission: eXTP

PACS number(s): 95.55.Ka, 95.85.Nv, 95.75.Hi, 97.60.Jd, 97.60.Lf

Citation: S.-N. Zhang, A. Santangelo, Y. Xu, H. Feng, F. Lu, Y. Chen, M. Ge, K. Nandra, X. Wu, M. Feroci, M. Hernanz, C. Liu, H. He, Y. Wang, W. Jiang, W. Cui, Y. Yang, J. Wang, W. Li, H. Li, Y. Du, X. Liu, B. Meng, X. Wen, A. Zhang, J. Ma, M. Li, G. Li, L. Qi, J. Sun, T. Luo, H. Liu, X. Liu, F. Zhang, L. Luo, Y. Zhu, Z. Zhao, L. Sun, X. Yang, Q. Wu, J. Jiang, H. Shi, J. Liu, Y. Xu, S. Yang, L. Zhang, D. Han, N. Gao, J. Huo, Z. Zhang, H. Wang, X. Zhao, S. Wang, Z. Li, Z. Bao, Y. Liu, K. Wang, N. Wang, B. Wang, L. Wang, D. Wang, F. Ding, L. Sheng, P. Qiang, Y. Yan, Y. Liu, Z. Wu, Y. Liu, H. Chen, Y. Zhang, H. Liu, A. Altmann, T. Bechteler, V. Burwitz, C. Fiorini, P. Friedrich, N. Meidinger, R. Strecker, L. Baldini, R. Bellazzini, R. Bonino, A. Frassà, L. Latronico, S. Maldera, A. Manfreda, M. Minuti, M. Pesce-Rollins, C. Sgrò, S. Tugliani, G. Pareschi, S. Basso, G. Sironi, D. Spiga, G. Tagliaferri, A. Tykhonov, S. Paltani, E. Bozzo, C. Tenzer, J. Bayer, Y. Tuo, H. Liu, Y. Zhang, Z. Cai, H. Liu, W. Chen, C. Wang, T. He, Y. Chen, C. Qiu, Y. Zhang, J. Feng, X. Zhu, H. Zhou, S. Zheng, L. Song, H. Shi, J. Wang, S. Jia, Z. Jiang, X. Li, H. Zhao, J. Guan, J. Zhang, C. Li, Y. Huang, J. Liao, Y. You, H. Zhang, W. Wang, S. Wang, G. Ou, H. Hu, J. Shi, T. Cui, X. Jiang, Y. Cheng, H. Li, Y. Xu, S. Zane, C. Bambi, Q. Bu, S. Dall'Osso, A. De Rosa, L. Gou, S. Guillot, L. Ji, A. Li, J. Mao, A. Patruno, G. Stratta, R. Taverna, S. Tsygankov, P. Uttley, A. L. Watts, X. Wu, R. Xu, S. Yi, G. Zhang, L. Zhang, W. Zhao, and P. Zhou, The enhanced X-ray Timing and Polarimetry mission—eXTP for launch in 2030, *Sci. China-Phys. Mech. Astron.* **68**, 119502 (2025), <https://doi.org/10.1007/s11433-025-2786-6>

1 Introduction

The enhanced X-ray Timing and Polarimetry mission—eXTP is a scientific space mission designed to study the state of matter under extreme conditions of density, gravity and magnetism [1-3]. Primary goals are the determination of the equation of state of matter at supra-nuclear density, the measurement of quantum electro-dynamics (QED) effects in the radiation emerging from highly magnetized stars, and the study of matter dynamics in the strong-field regime of gravity. The matter inside neutron stars (NSs), the space-time close to black holes (BHs), and the extremely magnetized vacuum close to magnetars are among the uncharted territories of fundamental physics. The eXTP mission will revolutionize these areas of fundamental research by high-precision X-ray measurements of NSs across the magnetic field scale and BHs across the mass scale. In addition to investigating fundamental physics, eXTP will be a very powerful observatory for the time-domain and multi-messenger astronomy in the 2030s, as well as providing observations of unprecedented quality on a variety of galactic and extragalactic objects. The eXTP science case is described in the other five white papers included in this special issue [4-8]. They address the four main scientific objectives of the mission and the observatory science. These are updated substantially from the white papers published in 2019 [9-12], to account for the rapid developments of the field over the past several years and the new mission profile described in the

present paper.

The eXTP mission is an enhanced version of the Chinese X-ray Timing and Polarimetry mission (XTP) [13], which in 2011 was selected and funded for a Phase 0/A study as one of the background concept missions in the Strategic Priority Space Science Program of the Chinese Academy of Sciences (CAS). Also in 2011, the Large Observatory for Timing (LOFT) mission concept [14, 15] was selected for an assessment study in the context of the ESA's Announcement of Opportunity for the third of the medium size missions (M3) foreseen in the framework of the Agency's Cosmic Vision program. The LOFT study was carried out in 2011-2014 by a consortium of European institutes. Eventually, the exoplanetary mission PLATO [16], considered more well timed, was selected as the ESA Cosmic Vision M3 mission. Following this, in 2015, the European LOFT consortium and the Chinese team merged the concepts of the LOFT and XTP missions, thus starting the eXTP project.

The mission completed an extended Phase A study in 2019 and a Phase B study in 2023, respectively. Due to the uncertainty in the availability of the expected European contributions, the mission was reconfigured near the end of 2023 to the current new baseline. The eXTP mission, based on the new baseline, was then approved by CAS in early 2024, approved at the national level in early 2025, and adopted in the middle of 2025 for launch in early 2030.

According to the adopted mission profile, the large area

detector (LAD, a large array of collimated detectors made of silicon drift detectors (SDDs)) and the wide field monitor (WFM, six modules of 1.5-D coded mask imager with SDDs as the pixelated detector planes) are not in the baseline. Both LAD and WFM are the main instruments of the LOFT mission [14, 15] and also the proposed European contributions to the previous baseline of the eXTP mission [2, 3]. In addition, the number of telescopes of the spectroscopy focusing array (SFA) and polarimetry focusing array (PFA) has been reduced from 9 to 6 and from 4 to 3, respectively, to facilitate deployment using a smaller, more cost-effective launch vehicle; the focal plane camera of one of the six SFA telescopes is replaced by a pnCCD (charge coupled device) camera, while the other five still use the original SDDs. The baseline orbit has been modified from a near-equatorial low-Earth orbit (LEO) to a high elliptical orbit (HEO) to enhance observational efficiency. However, a LEO configuration remains a viable alternative. A Wide Field and Wideband Camera (W2C) is considered as a secondary instrument to partially mitigate the loss of WFM capabilities. The key performance parameters of the eXTP satellite's current design are summarized in Table 1 [17-23], with comparative metrics from other flagship X-ray observatories listed for contextual benchmarking.

The eXTP consortium is led by the Institute of High Energy Physics (IHEP) of the CAS. In total, more than 200 scientists in more than 80 institutions from 17 countries are members of the eXTP instrument teams and science working

groups. In this paper, we present: (1) a summary of the scientific objectives of the eXTP mission in sect. 2; (2) the technological implementation and expected performance characteristics of the scientific payload instruments in sect. 3; and (3) the key operational elements and functional architecture of the mission in sect. 4.

2 Scientific objectives of the eXTP mission

The scientific objectives of eXTP can be divided into five themes: (1) to investigate the equation of state (EoS) of ultra-dense matter in NSs, presented in detail in White Paper 2 (WP2, [4]); (2) to understand black holes by probing strong gravity regions through synergistic X-ray spectral, timing, and polarimetric observations, presented in details in White Paper 3 (WP3, [5]); (3) to resolve some long-standing questions about QED effects and radiative processes in the strong magnetic fields, presented in details in White Paper 4 (WP4, [6]); (4) to play a key role in the era of time-domain and multi-messenger astronomy, presented in details in White Paper 5 (WP5, [7]); and (5) to provide observations of unprecedented quality on a variety of galactic and extragalactic objects, as a very powerful observatory for astrophysics, presented in details in White Paper 6 (WP6, [8]). Scientific goals in themes 1-4 are the core objectives of the current eXTP mission, expanded from the original themes 1-3 [2], which have

Table 1 The key instrument performances of the current design of the eXTP satellite and other main current/future missions for comparison^{a)}

| Instrument | A_{eff} (cm^2) | E (keV) | T | P_{MDP} (MDP) | θ | F_{bkg} ($\text{cts s}^{-1} \text{cm}^{-2} \text{keV}^{-1}$) | PE (cts s^{-1}) |
|---------------------------|---|--------------|---|---------------------------|-------------------------|--|---------------------------------|
| eXTP/SFA-T | 2750@1.5 keV 1670@6 keV | 0.5-10 | 10 μs | No | $\sim 1'$ | $< 1 \times 10^{-2}$ | No |
| eXTP/SFA-I | 550@1.5 keV 330@6 keV | 0.5-10 | 50 ms (full) 240 μs (timing) | No | $\sim 1'$ | $\sim 10^{-2}$ | 3 (FF) |
| eXTP/PFA | 250@3 keV | 2-8 | 10 μs | 2% (100 ks) | $\sim 30''$ | $< 10^{-2}$ | No |
| eXTP/W2C | 160@60 keV | 30-600 | ≤ 1 ms | No | $< 1^\circ$ | $\sim 10^{-2}$ | No |
| RXTE/PCA [17] | 6500@6 keV ~ 3000 @3 keV | 2-60 | 1 μs | No | $\sim 1^\circ$ | $\sim 10^{-1}$ | No |
| Chandra (ACIS-I) [18] | ~ 600 @1.5 keV | 0.2-10 | 3.2 s | No | $\sim 0.5''$ | $\sim 10^{-3}$ | 0.03 |
| XMM-Newton (EPIC-PN) [19] | ~ 1500 @1.5 keV ~ 900 @6 keV | 0.15-12 | 30 μs (timing) | No | $\sim 15''$ | $\sim 10^{-3}$ | 8 |
| NICER [20] | ~ 1900 @1.5 keV ~ 600 @6 keV | 0.2-12 | < 0.3 μs | No | $\sim 6'$ (non-imaging) | $\sim 10^{-2}$ | No |
| IXPE [21] | ~ 60 @3 keV | 2-8 | ~ 10 μs | $\sim 3\%$ (100 ks) | $\sim 30''$ | $< 10^{-2}$ | No |
| EP-FXT [22] | ~ 600 @1.25 keV | 0.5-10 | ~ 44 μs | – | $\sim 30''$ | $< 10^{-2}$ | 5 (FF) |
| NewAthena/X-IFU [23] | ~ 5200 @1 keV | 0.2-12 | 10 μs | No | $\sim 9''$ | $\sim 10^{-3}$ | – |
| NewAthena/WFI [23] | ~ 8600 @1 keV | 0.2-15 | 80 μs (fast) 160 μs (normal) | No | $\sim 9''$ | $\sim 10^{-3}$ | – |

a) These parameters includes effective area (A_{eff}), energy range (E), timing resolution (T), polarimetric sensitivity (minimum detectable polarization, P_{MDP}), angular resolution (θ), background level (F_{bkg}) and pile-up limit (PE).

driven the eXTP baseline mission design and its evolution.

WP2 focuses on how to determine the relation between the mass and radius of NSs with the eXTP observations, which are the key elements to studying EoS. Several methods of mass and radius measurements are proposed by different phenomena including: (1) mass and radius measurements by pulse profile modeling of rotation powered milli-second pulsars (MSPs); (2) mass and radius measurements by pulse profile modeling of accretion-powered MSPs together with the polarized information; (3) mass and radius constraints by thermonuclear burst cooling tails, accretion disk dynamics and cooling curve of MSPs; (4) the inner structure of NS revealed by glitches; and (5) EoS constraints with other phenomena and methods.

WP3 studies how to understand black holes and the physics in strong gravity with eXTP observations. Leveraging its advanced instruments, eXTP will enable unprecedented precision in measuring black hole parameters and testing fundamental physics. The scientific objectives include: (1) spin and mass measurements using relativistic reflection spectroscopy (e.g., Fe K_{α} line profiles), thermal continuum fitting or polarization data; (2) measuring spins and masses of supermassive black holes (SMBHs) with quasi-periodic oscillations (QPOs), X-ray reverberation in super-Eddington accretion flows, and track orbital hotspots; (3) testing general relativity by analyzing possible deviations from Kerr metrics; and (4) accretion physics, such as disk-corona dynamics and coronal geometry, with time-resolved spectral-timing techniques and polarization data.

WP4 discusses how to resolve some long-standing questions about QED effects and radiative processes in strong magnetic fields with eXTP observations. The primary science goals include: (1) testing QED predictions, such as vacuum birefringence, through polarization studies of magnetars and neutron stars with ultra-strong magnetic fields (10^{13} - 10^{15} G); (2) probing magnetic field topology and surface emission mechanisms in magnetars and accreting X-ray pulsars (XRPs) via phase-resolved polarimetry and spectroscopy; (3) investigating accretion dynamics in strongly magnetized systems, including transitions between sub/super-critical accretion regimes and the geometry of accretion columns; (4) characterizing magnetar outbursts, glitches, and their connection to fast radio bursts (FRBs); and (5) exploring extreme accretion in pulsating ultraluminous X-ray sources (PULXs).

WP5 demonstrates the roles eXTP may play in the fast rising time-domain and multi-messenger astronomy through its advanced instruments. Key science topics include: (1) probing gravitational wave (GW) counterparts such as neutron star/black hole mergers and extreme mass-ratio inspirals (EMRIs) to constrain neutron star equations of state

and black hole spins, studying SMBHs via X-ray timing and Fe K_{α} line diagnostics, and exploring gamma-ray burst (GRB) physics through polarization measurements to distinguish synchrotron versus photospheric emission mechanisms and test quantum gravity effects via X-ray polarimetry; (2) investigating magnetar bursts, FRBs, and long-period radio transients to unravel magnetic field dynamics and emission origins; (3) monitoring tidal disruption events (TDEs) to understand super-Eddington accretion and relativistic jet formation; and (4) observation of core-collapse supernovae, TeV-active galactic nuclei, and potential neutrino-associated transients.

WP6 showcases that eXTP, as a very powerful observatory for astrophysics, will provide observations of unprecedented quality on a variety of galactic and extragalactic objects. The observatory science objectives may include: characterizing stellar coronae and transient phenomena such as flares and coronal mass ejections, probing magnetic turbulence and particle acceleration in supernova remnants and pulsar wind nebulae, investigating accretion physics across diverse systems (e.g., Cataclysmic Variables (CVs), X-ray binaries (XRBs), active galactic nuclei (AGNs)), exploring super-Eddington accretion in ultraluminous X-ray sources (ULXs), and advancing X-ray pulsar-based timing techniques.

3 The scientific payload

An illustration of the current design of the eXTP satellite is shown in Figure 1. The scientific payload of the mission consists of two main and possibly one secondary instruments: the SFA (sect. 3.1), the PFA (sect. 3.2), and the W2C (sect. 3.3).

3.1 Spectroscopy focusing array—SFA

The spectroscopic focusing array (SFA) comprises six Wolter-I grazing-incidence X-ray telescopes designed for

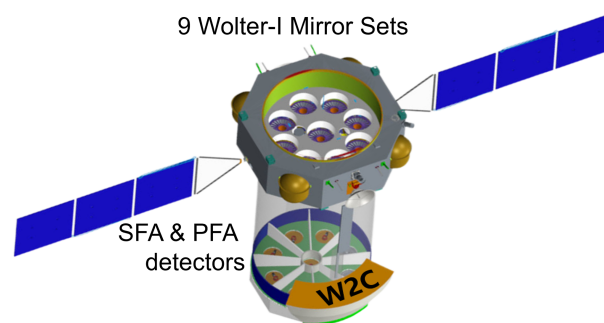


Figure 1 Illustration of the eXTP satellite. The science payload consists of two main instruments and a secondary instrument: the focused SFA and PFA telescopes arrays, and the W2C to monitor a large fraction of the sky over a broad energy band.

spectral, timing, and imaging observations in the 0.5 to 10 keV energy range. Each telescope assembly includes the mirror module, the electron deflector, the filter wheel, and the focal plane camera. Five of the focal plane cameras are equipped with SDDs, and their corresponding telescopes are designated SFA-T (where “T” denotes “Timing”), reflecting the SDDs’ excellent timing resolution. A schematic of the SFA-T telescope design is presented in Figure 2. The sixth telescope features a pnCCD focal plane camera, analogous to those employed in eROSITA [24] and Einstein Probe [22], providing enhanced point-source sensitivity (via reduced background) and superior imaging performance. This unit is designated SFA-I (where “I” signifies “Imaging”). The focal plane detector modules for both the SFA-T and SFA-I detectors will be developed and contributed to the eXTP project by the Max Planck Institute for Extraterrestrial Physics (MPE). The sensor chips are fabricated by the Semiconductor Laboratory of the Max Planck Society (MPG-HLL). The total effective area of SFA is expected to be larger than $\sim 3300 \text{ cm}^2$ at 1.5 keV and $\sim 2000 \text{ cm}^2$ at 6 keV, and the field of view (FoV) is 18 arcmin. Each SFA-T telescope includes a 19-cell SDD array, whose energy resolution is better than 180 eV at 6 keV. The time resolution is 10 μs , and the dead time is expected to be less than 5% for a source flux of approximately 1 Crab. The angular resolution must be less than 1 arcmin (half-power diameter, HPD). To meet the requirements, the working temperature of the mirror modules must be stable at $(20 \pm 2)^\circ\text{C}$. An electron deflector is installed at the bottom of the mirror module to reduce the particle background.

3.1.1 Optics

Since they are based on very similar concepts, in this section, we discuss the optics of both the SFA and the PFA together. Nine X-ray grazing-incidence Wolter I (parabola + hyperbola) optics modules will be implemented onboard eXTP;

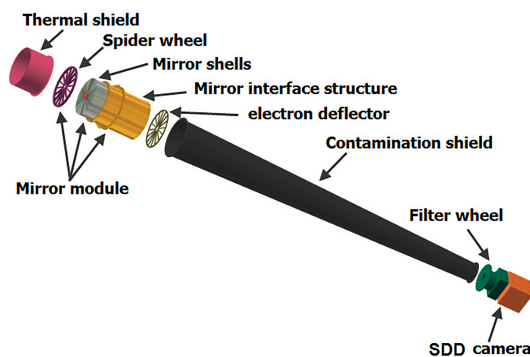


Figure 2 The schematic structure of one of the SFA telescopes. Taken from the previous eXTP mission paper [2].

the mirror technique implemented is nickel replication, which has already been successfully used for high-throughput X-ray telescopes with good angular resolution, such as for the BeppoSAX [25], XMM-Newton [19], Swift [26], eROSITA [24], and ART-XC telescopes onboard the Spektr-Roentgen-Gamma Mission [27], the IXPE [21, 28] polarimetric mission, and the FXT telescope aboard the Einstein Probe mission [22]. The SFA includes six optic modules, while three optic modules are used for the PFA. The expected collecting area of each telescope is $A_{\text{optics}} \gtrsim 820 \text{ cm}^2$ (SFA) and $\gtrsim 800 \text{ cm}^2$ (PFA) at 3 keV, and $A_{\text{optics}} \gtrsim 550 \text{ cm}^2$ at 6 keV. The requirement for the angular resolution of the PFA optics is $\leq 30 \text{ arcsec}$ (HPD)@3 keV, more demanding than the angular resolution of 1 arcmin (HPD)@1.5 keV required for the SFA optics. For both types of telescope, the focal length reference value is 525 cm. The maximum diameter of the mirror shells is about 510 mm, constrained by the envelope of less than 600 mm in diameter for a single mirror. In Table 2, we list the main parameters of the SFA and PFA optics.

Figure 3 shows the expected collecting area A_{optics} of a

Table 2 The main parameters of the SFA and PFA baseline optics

| Parameters | For one telescope |
|----------------------------------|----------------------------------|
| Focal length | 5.25 m |
| Aperture | $\leq 510 \text{ mm}$ (diameter) |
| Envelope | $\leq 600 \text{ mm}$ (diameter) |
| A_{optics} of SFA | $\geq 820 \text{ cm}^2$ @1.5 keV |
| A_{optics} of PFA | $\geq 800 \text{ cm}^2$ @3 keV |
| A_{optics} of SFA & PFA | $\geq 550 \text{ cm}^2$ @6 keV |
| Energy range | 0.5-10 keV |
| Field of view | $18' \times 18'$ |
| Angular resolution SFA | $\leq 1'$ (HPD)@1.5 keV |
| Angular resolution PFA | $\leq 30''$ (HPD)@3 keV |

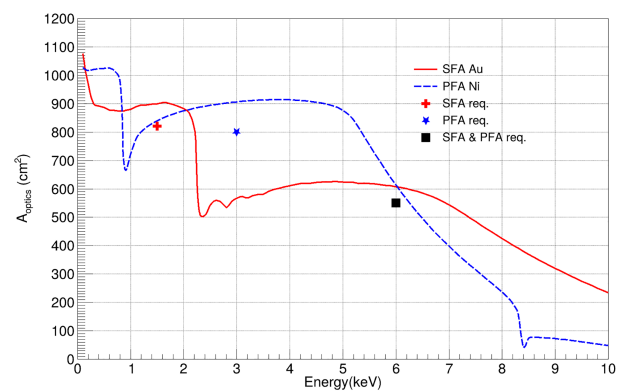


Figure 3 On-axis collecting area A_{optics} expected for the eXTP X-ray optics based on Nickel electroforming (a single mirror module), with different coatings. For SFA, the gold film is selected with 100 nm thickness. For PFA, nickel is directly employed as the coating.

mirror module with different coatings. For SFA, the gold film is selected with 100 nm thickness as the reflective material based on the following considerations: (1) the gold film exhibits stable reflectivity characteristics in the 0.2-10 keV energy range; (2) its thermal expansion coefficient closely matches that of nickel, facilitating mold release in the electroformed nickel gold-plating process; and (3) the gold-plating process offers high maturity and reliability. For PFA, nickel is directly employed as the reflective material to fulfill its requirements for effective area and quality factor. Figure 4 shows the mirror vignetting function.

3.1.2 SFA-T detectors

The scientific objectives of the SFA require a detector with high count rate capability and time resolution, along with excellent spectroscopic performance. The energy resolution must be better than 180 eV (FWHM at 6 keV) until the end of the mission after 8 years of operation, and the time resolution must be less than 10 μ s. The main specifications for SFA-T (5 telescopes with SDD detectors) are listed in Table 3.

The focal plane detector for each SFA-T telescope consists

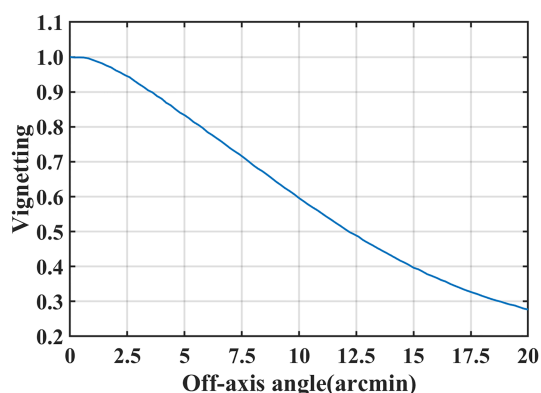


Figure 4 Vignetting function at 1.5 keV of the eXTP X-ray optics based on Nickel electroforming with Au coating.

Table 3 SFA-T specifications (5 telescopes with SDD at focal plane), where both HPD and W90 (width of the point spread function enclosing 90% reflected photons) are at 1.5 keV

| Indicator | Requirement |
|-----------------------------------|--|
| Total effective area | $\geq 2750 \text{ cm}^2 @ 1.5 \text{ keV}$ |
| (within $E \pm 0.5 \text{ keV}$) | $\geq 1670 \text{ cm}^2 @ 6 \text{ keV}$ |
| Energy range | 0.5-10 keV |
| Energy resolution (FWHM) | $\leq 180 \text{ eV} @ 6 \text{ keV}$ |
| Field of view | 18' (diameter) |
| SDD pixel size | 6.4 mm (4.2') |
| Angular resolution | $\leq 1'$ (HPD), $3'$ (W90) |
| Time resolution | $\leq 10 \mu\text{s}$ |
| Absolute timing accuracy | $\leq 2 \mu\text{s}$ |
| Dead time | $\leq 5\% @ 1 \text{ Crab}$ |

of an SDD sensor arranged in 19 hexagonal cells, with readout provided by custom ASICs, three of which are needed for each 19-cell SDD [29].

This configuration meets the aforementioned requirements (see Figure 5). Compared with CCDs, SDDs allow a much faster readout. The detector geometry ensures that the vast majority of source photons are focused onto the inner 7 cells of the array, whereas the cells of the outermost ring are used to accurately determine the background. Thus, the side length of a hexagonal cell has been determined to be 3.2 mm, given the expected angular resolution of the optics, a trade-off between the number of pixels and some sampling of the mirror's response. The sensor has a 450 μ m sensitive thickness, which delivers excellent quantum efficiency throughout the SFA energy range. The signal processing chain of each SDD cell includes a charge-sensitive preamplifier, a fast shaper, and a slow shaper with sample-and-hold circuit. A field programmable gate array (FPGA) based back-end electronics (BEE) module is implemented to control the front-end electronics (FEE) and read the digitized data from the analog-to-digital converters (ADCs).

A filter wheel is located above the detector, with four positions corresponding to 4 operational modes. (1) Open filter. It is used in ground tests and weak sources observations. (2) Calibration. A Fe-55 radioactive source is used for in orbit calibration. (3) Optical blocking filter. This filter, which consists of a 400 nm polyimide and a 200 nm aluminum film, is used to block visible and ultra-violet (UV) light. It also prevents contamination of the detector. (4) Closed

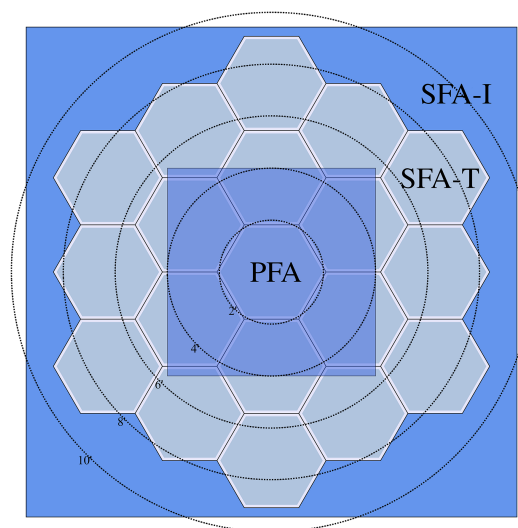


Figure 5 Comparison between the FoVs of SDD (grey color, each of the 19 hexagon cells has a side length of 3.2 mm and a sensitive thickness of 450 μ m), pnCCD (blue color) and GPD (blue color in the center) cameras. Circles denote the angular scale in 2' increments from 2' to 10'. The FoVs of PFA, SFA-T and SFA-I are thus 8' \times 8' (square), 18' in diameter (circle), and slightly larger than 18' \times 18' (square), respectively.

filter. A metal shutter is used to measure the internal background and prevents the detector from being damaged during launch and extreme solar events. To compensate for particle damage to the SDDs, especially due to protons, a temperature of -55°C is expected during the operation of the detectors. Temperature stability of $\pm 0.5^{\circ}\text{C}$ is also required.

Please refer to refs. [2, 3] for more details on SDDs and electronics.

3.1.3 SFA-I detector

The SFA-I pnCCD camera supports three distinct observation modes to address various scientific requirements. The key technical specifications include a $28.8 \times 28.8 \text{ mm}^2$ detector active area (5.25 m focal length) with $75 \times 75 \mu\text{m}^2$ pixels ($2.95''/\text{pixel}$), where pileup constraints dictate mode selection for bright source observations. The choice of a $\sim 3''$ pixel size given the $1'$ HPD mirror module requirement is not an optimal solution. It is done so because we simply decided to replace the SDD focal plane camera with the existing pnCCD camera used for EP/FXT. However, we will select the SFA mirror module with the best angular resolution for SFA-I, to better match the $\sim 3''$ pixel size of the pnCCD camera. The full frame mode serves wide-field surveys and multiobject spectroscopy, while the windowed mode facilitates time-resolved studies of medium-brightness sources. The timing mode specializes in millisecond variability analysis of bright transients. The main specifications for SFA-I (1 telescope with a pnCCD camera) are listed in Table 4. The comparison between the FoVs of the SDD, pnCCD and gas pixel detector (GPD, for PFA) cameras is shown in Figure 5. The FoV of SFA-I (with pnCCD) is the largest (18 arcmin) and thus covers that of SFA-T and PFA, allowing SFA-I to provide simultaneous spectra (and images) of all sources in the FoVs of SFA-T and PFA.

In full-frame mode (384×384 pixels) it provides an $18' \times 18'$ field of view with $2.95''$ per pixel resolution, simultaneously acquiring 0.5-10 keV energy spectra while monitoring source variability at 50 ms time resolution and localizing targets with $< 10''$ accuracy (90% confidence). This mode supports observations up to 3 mCrab brightness under 10% pile-up conditions. The windowed mode (61×128 pixels), as shown in Figure 6 (left), enhances the time resolution to < 3 ms (2.2 ms cycle), optimized for medium brightness point sources with observational limits of 60-70 mCrab. For bright targets, the timing mode (384×128 pixels fast readout), as shown in Figure 6 (right), enables $240 \mu\text{s}$ time resolution using 1D imaging (HPD $30''$), accommodating sources up to 700 mCrab. Inheriting EP-FXT technology, SFA-I combines imaging, spectroscopy, and timing capabilities.

Table 4 SFA-I specifications (1 telescope with pnCCD camera at focal plane), where both HPD and W90 are at 1.5 keV

| Indicator | Requirement |
|-----------------------------------|---|
| Total effective area | $\geq 550 \text{ cm}^2 @ 1.5 \text{ keV}$ |
| (within $E \pm 0.5 \text{ keV}$) | $\geq 330 \text{ cm}^2 @ 6 \text{ keV}$ |
| Energy range | 0.5-10 keV |
| Energy resolution (FWHM) | $\leq 180 \text{ eV} @ 1.5 \text{ keV}$ |
| Field of view | $18' \times 18'$ |
| Angular resolution | $\leq 1'$ (HPD), $3'$ (W90) |
| | $\leq 50 \text{ ms}$ (full frame) |
| Time resolution | $\leq 240 \mu\text{s}$ (timing mode) |
| | $\leq 3 \text{ ms}$ (windowed mode) |

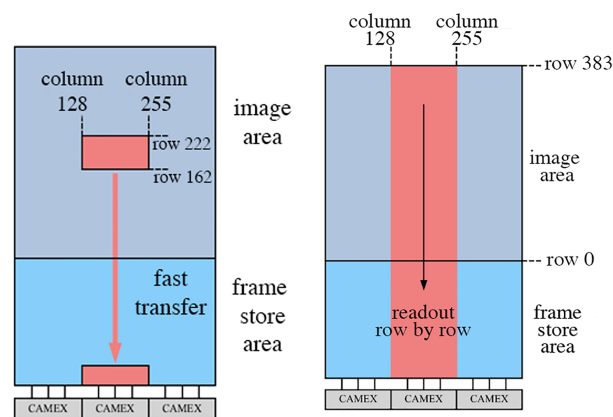


Figure 6 Left: pnCCD windowed mode (61×128 pixels). Right: pnCCD timing mode (384×128 pixels fast readout).

The pnCCD within the FoV of the telescopes simultaneously receives signals from X-ray photons and charged particles. However, it is usually difficult to distinguish between the signals of X-ray photons and charged particles with the same energy depositions. The frame's storage section is also part of the pnCCD, but it is not exposed to the telescope's FoV, and therefore only receives charged particles but does not receive X-ray photons. After half of an exposure, the charge in the storage area due to energy depositions of charged particles is transferred out. At the end of the exposure, the charge from the pixels in the FoV is transferred into the storage area and then transferred out from there. Consequently, the charge first transferred out of the storage area can be used to determine the in-orbit particle background spectra and counting rates. The peripheral FoV regions, where no source is detected, are used for diffuse X-ray background measurements. Compared with SFA-T (with SDD arrays), while sharing identical energy resolution and effective area (from common $450 \mu\text{m}$ depletion layer detectors and focusing mirrors), SFA-I demonstrates distinct advantages and limitations. The SDD array has 19 pixels, and the outer ring of 12 pixels is used for estimating the background. However, unknown contaminating sources within

the FoV cannot be identified and removed cleanly, resulting in systematic errors of the background modeling. The imaging capability of pnCCD and nearly the same energy response with SDD allow pnCCD to identify and characterize any contaminating sources within the FoV, which serves as an input for the background modeling of SFA-T with SDDs.

The much cleaner background of SFA-I makes it 3 times more sensitive than that of an SFA-T telescope for faint sources, as shown in Figure 7; no comparison with the PFA sensitivity is made since the key requirement of PFA is its minimum detectable polarization degree. In WP2 [4], some simulations are made to show how SFA-I may improve the estimate of the mass and radius of a NS by providing the simultaneous spectrum of a contaminating source in the FoV of SFA-T. However, SFA-I exhibits a worse timing resolution compared with SDD and faces saturation challenges when observing bright sources such as BH and NS X-ray binary outbursts, as well as X-ray bursts of neutron stars and the bright early X-ray afterglows of gamma-ray bursts.

The total effective area of the SFA (SFA-T+SFA-I), taking into account the detector efficiency and filters, is shown in Figure 8, compared with that of the wide field imager (WFI) of the NewAthena, XMM-Newton and NICER missions [19,20,23].

3.2 Polarimetry focusing array—PFA

The PFA consists of three identical telescopes optimized for X-ray imaging polarimetry, sensitive in the energy range of 2-8 keV. In synergy with the SFA, the PFA offers spatial, energy, and/or temporal resolved X-ray polarimetry at high sensitivity. The main PFA specifications are listed in Table 5.

The PFA optics are described in sect. 3.1. Figure 9 provides an exploded view of the PFA detector unit (DU), which consists of three key components: the calibration and filter wheel in the top, the focal plane detector in the middle, and the back-end electronics at the bottom.

3.2.1 Calibration and filter wheel

The calibration and filter wheel (CFW), shown in Figure 10, is to house five calibration sources and a set of filters (gray, open, and closed).

The calibration sources will be used to calibrate or monitor the performance of the focal plane detector throughout the mission lifetime, including gain, energy resolution, modulation factor, and spurious modulation. Each contains a ^{55}Fe radioactive isotope, which has a half-life of 2.7 years. Cal A and Cal B generate polarized X-rays via Bragg diffraction using different crystals. These two sources are designed to

irradiate the entire sensitive area of the GPD and are mainly used to monitor or calibrate modulation factors. Cal A pro-

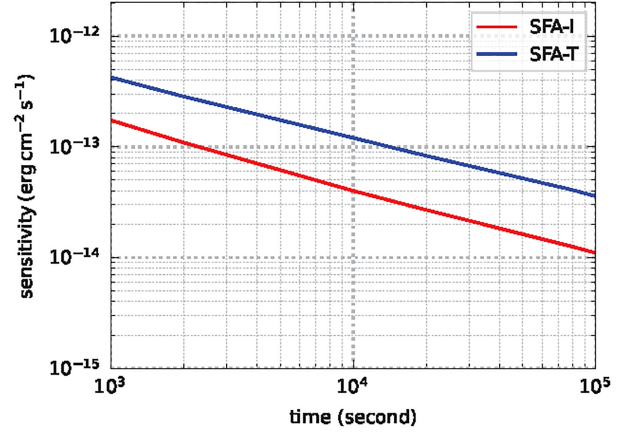


Figure 7 Sensitivity (0.5-10 keV) comparison between one SFA-T telescope and one SFA-I. The improved sensitivity of SFA-I is solely due to its smaller pixel size, so that lower background counts are recorded in the central pixels, which receive most of the X-ray photons from the target point source. Note that the diffusion limits in some crowded fields due to the limited angular resolutions of the telescopes are not considered here, though negligible for SFA-I and not serious for SFA-T.

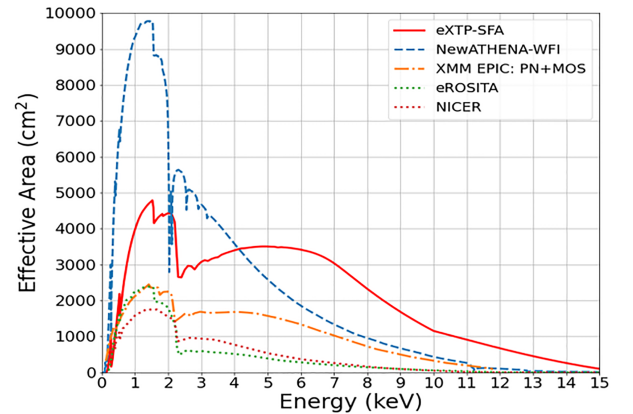


Figure 8 The total effective area of the SFA (SFA-T+SFA-I), taking into account the optics and detector efficiency, in comparison with that of the WFI of the NewAthena, XMM-Newton, and NICER missions.

Table 5 PFA specifications (3 telescopes with GPD at focal plane)

| Indicator | Requirement |
|---------------------------------|--|
| Total effective area | $\geq 180 \text{ cm}^2 @ 3 \text{ keV}$ |
| Energy range | 2-8 keV |
| Energy resolution (FWHM) | $\leq 1.8 \text{ keV} @ 6 \text{ keV}$ |
| Field of view | $9.8' \times 9.8'$ |
| Angular resolution | HPD $\leq 30'' @ 3 \text{ keV}$ |
| Time resolution | $\leq 10 \mu\text{s}$ |
| Dead time | $\leq 10\% @ 1 \text{ Crab}$ |
| Polarization modulation factor | $\geq 50\% @ 6 \text{ keV}$ |
| Minimum detectable polarization | $\leq 3\% (1 \text{ mCrab}, 10^6 \text{ s})$ |

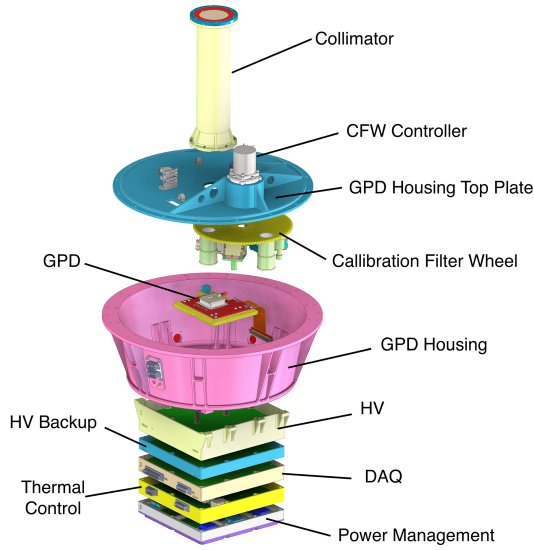


Figure 9 An exploded view of the PFA detector unit.

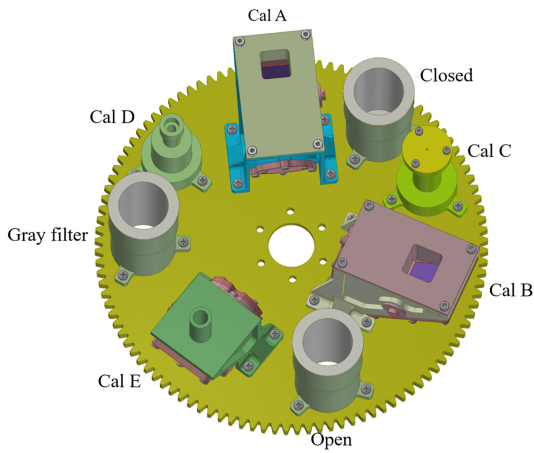


Figure 10 A schematic drawing of the filter and calibration wheel.

vides two energy lines at 3 and 5.9 keV, while Cal B offers an additional line at 4.5 keV. Cal C, Cal D, and Cal E are unpolarized sources. Cal C is a collimated 5.9 keV source, with a beam diameter of less than 5 mm, to monitor the gain, energy resolution, and spurious modulation in the central region of the GPD. In contrast, Cal D and Cal E are uncollimated and emit two lines at 5.9 and 1.7 keV, enabling performance monitoring across the entire sensitive area. Table 6 summarizes the characteristics of these calibration sources.

The gray filter is intended for observations of very bright sources that may produce high count rates and lead to severe pile-up. The preliminary design consists of a Kapton foil with a thickness of 100 μm , coated with 100 nm aluminum on both sides. Its transmission is shown in Figure 11. The filter will attenuate low-energy photons, with a transmission of about 40% at 4 keV.

Table 6 PFA in-orbit calibration sources

| Name | Description | Rate |
|-------|--|--|
| Cal A | Polarized, $15 \times 15 \text{ mm}^2$ | $> 5.2 \text{ c s}^{-1}$ @ 3 keV $> 1.6 \text{ c s}^{-1}$ @ 5.9 keV |
| Cal B | Polarized, $15 \times 15 \text{ mm}^2$ | $> 2.5 \text{ c s}^{-1}$ @ 4.5 keV |
| Cal C | Unpolarized, diameter $< 5 \text{ mm}$ | $> 23.1 \text{ c s}^{-1}$ @ 5.9 keV |
| Cal D | Unpolarized, $15 \times 15 \text{ mm}^2$ | $> 23.1 \text{ c s}^{-1}$ @ 5.9 keV |
| Cal E | Unpolarized, $15 \times 15 \text{ mm}^2$ | $> 23.1 \text{ c s}^{-1}$ @ 1.7 keV |

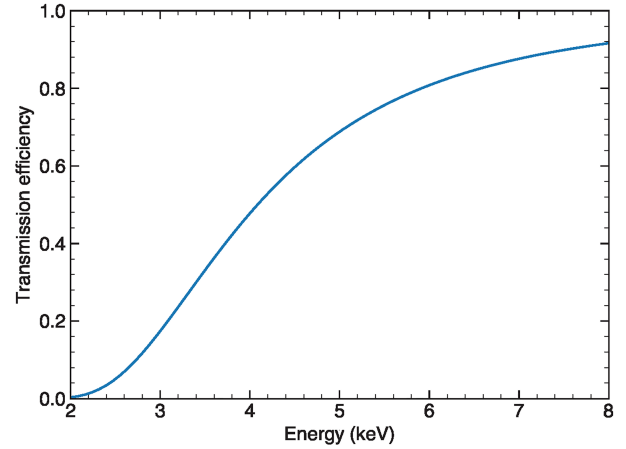


Figure 11 Transmission efficiency of the gray filter designed for PFA.

3.2.2 Detectors and electronics

A GPD is adopted as the focal plane polarimeter for the PFA. It was originally developed by the INFN-Pisa group [30-33], and has been used in PolarLight [34,35] and IXPE [36]. With the GPD, one can measure the 2D ionization track of the photoelectron in the gas chamber and infer the polarization of the X-ray source by reconstructing the emission angle of the photoelectron. The main characteristics of the GPD designed for PFA are summarized in Table 7, and a schematic drawing of the detector is shown in Figure 12.

Table 7 Basic characteristics of the GPD for PFA

| Parameter | Value |
|-----------------------------------|--|
| Thickness of the Beryllium window | 50 μm |
| Thickness of the absorption gas | 10 mm |
| Thickness of the induction region | 0.8 mm |
| Active area | $15 \times 15 \text{ mm}^2$ |
| Readout pitch | 50 μm (hexagonal) |
| Gas mixture | Pure DME |
| Filling pressure | 0.8 atm |
| Drift field strength | 2 kV cm^{-1} |
| Induction field strength | 5 kV cm^{-1} |
| Operation temperature | (20-25) $^{\circ}\text{C} \pm 1^{\circ}\text{C}$ |

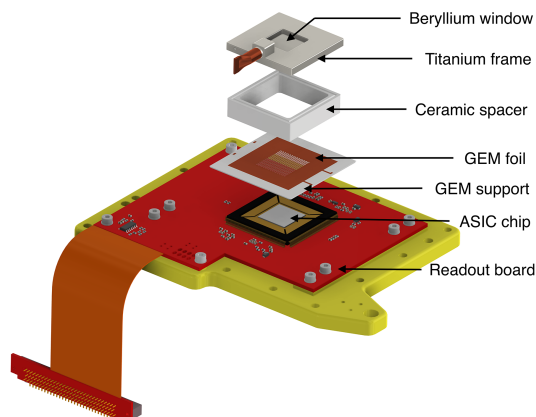


Figure 12 A schematic drawing of the GPD.

As shown in Figure 12, the GPD is a gas chamber sealed by a 50 μm thick Beryllium entrance window. The working gas is pure dimethyl ether (DME), which absorbs the incident X-rays and converts them to photoelectrons. A drift field of about 2 kV cm^{-1} is applied in the chamber to drive the secondary electrons ionized by the photoelectron to move towards the anode. To enable measurements with a sufficient signal-to-noise ratio, a gas electron multiplier (GEM) is mounted above the anode to multiply the number of electrons by a gain factor of a few hundred, which can be adjusted by the high voltage across the top and bottom layers of the GEM. The readout plane is mounted underneath the GEM. It is an ASIC chip [37-39] pixelated with a pitch of 50 μm , responsible for collection and measurement of the charges after multiplication. The ASIC has a dimension $1.5 \text{ cm} \times 1.5 \text{ cm}$, which defines the sensitive region of the detector. The readout noise is around $50 e^-$. The BEE is designed to control and operate the ASIC, drive the analog-to-digital conversion, organize and store the data, and communicate with the satellite. They also regulate the high-voltage modules, which are needed for the drift field and to power the GEM field.

The modulation factor, defined as the instrument's response to a fully polarized X-ray source, is one of the key parameters of an X-ray polarimeter. Figure 13 shows the measured modulation factors of the GPD across the 2-8 keV energy range.

It decreases with decreasing energy for two reasons. First, the Coulomb scattering of the photoelectron by the nucleus will randomize the emission angle and lower the modulation degree, which becomes more important at low energies. Second, because of the shorter range of the track at low energies, the reconstruction of the emission angle becomes more difficult and is limited by the finite pixel size.

The GPD was first launched into orbit with the PolarLight project and operated for 3 years [34, 35]. Then, it was used for the IXPE mission [36], which has been working in orbit

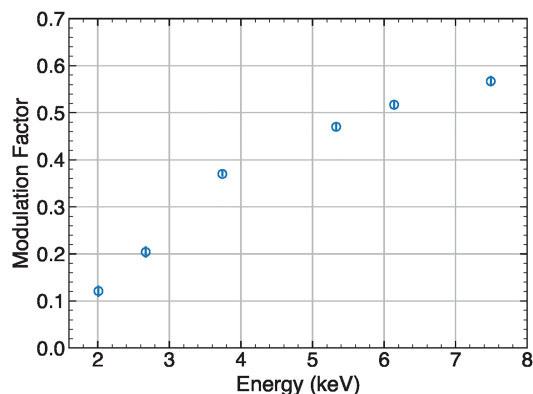


Figure 13 Measured modulation factors of the GPD.

for more than 3.5 years as of May 2025. One of the issues with the GPD is the spurious modulation, an instrument systematic that shows polarization-like modulations when observing a non-polarized source. This systematic can be calibrated out before launch. For IXPE, a dither pattern is employed during observation such that the focal spot covers a large area to further smooth out the systematics at different GPD regions. This approach can help reduce the calibration time. However, as eXTP has co-aligned SFA-T telescopes that have non-imaging SDD detectors, dithered observations are not preferred, unless the flux modulation caused by dithering in SFA-T can be modeled out effectively with the help of the co-aligned SFA-I and PFA with imaging capability. This issue remains to be studied during the Phase C development. Therefore, the calibration task for the PFA GPD is particularly challenging. The final calibration plan will be optimized on the basis of the actual spurious modulations of the GPD qualification model.

3.2.3 Sensitivity

The total effective area of the three PFA telescopes as a function of energy is shown in Figure 14, against the effective area of IXPE for comparison. The effective area of the PFA is about five times that of IXPE at 3 keV.

The sensitivity of the polarimeter is usually defined as the minimum detectable polarization (MDP), described as $\text{MDP} = \frac{4.29}{\mu \sqrt{SA}} \sqrt{\frac{SA+B}{t}}$, where μ is the modulation factor, A is the effective area, S is the source intensity in photons $\text{cm}^{-2} \text{s}^{-1}$, B is the background rate in the source aperture in counts s^{-1} , t is the exposure time, and 4.29 corresponds to a confidence level of 99%. In cases where the background is not important, the MDP can be approximated as $\text{MDP} = \frac{4.29}{\mu \sqrt{SA}}$. Thus, sensitivity is not only a function of the effective area, but is correlated with $\mu \sqrt{A}$. As one can see, the effective area peaks at about 2 keV while the sensitivity peaks at around 3 keV due to the increase of the modulation

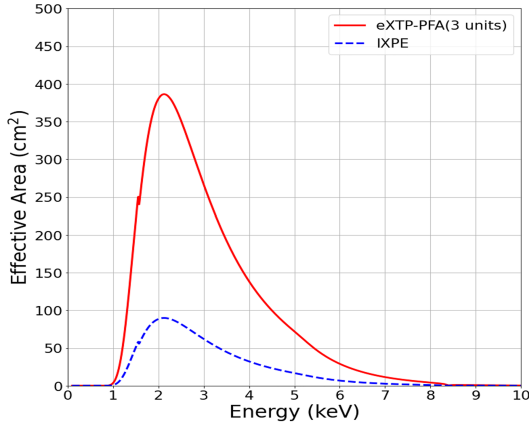


Figure 14 Total effective area of PFA and IXPE.

factor with energy.

The sensitivity of PFA can be approximately estimated, given a source with a crab-like spectrum. In the energy band of 2-8 keV, the mean modulation factor is ~ 0.23 weighted by the observed spectrum. In the case of negligible background, an exposure of 1 ks of the Crab nebula will result in an MDP of 2%. Sensitivities for observations with sources of different intensities and different exposure times can be scaled by simply using the equation for the MDP. We also note that the MDP quoted above indicates a detection at the confidence level 99% (a chance probability of 1% of having such a level of measurement from a fully unpolarized source), and more observation time is needed to achieve a precise measurement with a significance of 3σ or more [40].

3.3 Wide-field and wide-band camera—W2C

The FoV of the W2C is approximately 1500 square degrees (Full-Width Zero Response, FWZR), with an energy range of 30-600 keV; the main technical specifications are listed in Table 8. Its primary function is to discover new high-energy bursts and trigger rapid onboard autonomous follow-up observations of the SFA and PFA. As shown in Figure 1, W2C is located at the bottom of the satellite, with its FoV not overlapping with that of SFA and PFA. The schematic drawing of the W2C is shown in Figure 15 for illustration. When detecting and locating a transient source, it will send trigger requests to the satellite platform. If approved, the satellite will rapidly reorient to position the transient source at the center of the SFA and the PFA's FoV. The main features of W2C include:

- Coded-aperture imaging and localization. It uses random coding patterns combined with partial coding FoV technology to expand the FoV of the image while maintaining a high signal-to-noise ratio in fully coded regions. It implements background subtraction and inverse matrix calculation

Table 8 W2C specifications

| Indicator | Requirement |
|----------------------|---|
| Field of view | Full coding: $49^\circ \times 9.6^\circ$ |
| | Half coding: $60^\circ \times 16^\circ$ |
| Angular resolution | FWZR: $68^\circ \times 22^\circ$ |
| | $\sim 20'$ @ 30-100 keV |
| Positioning accuracy | $\sim 5'$ @ 30-100 keV |
| Effective area | $\sim 160 \text{ cm}^2$ @ 60 keV (normal incidence) |
| Sensitivity | $\sim 4 \times 10^{-7} \text{ erg cm}^{-2} \text{ s}^{-1}$ @ 10-1000 keV in 1 s |
| Energy range | 30-600 keV |
| Energy resolution | $\leq 30\%$ @ 60 keV |
| Time resolution | $\leq 25 \mu\text{s}$ |

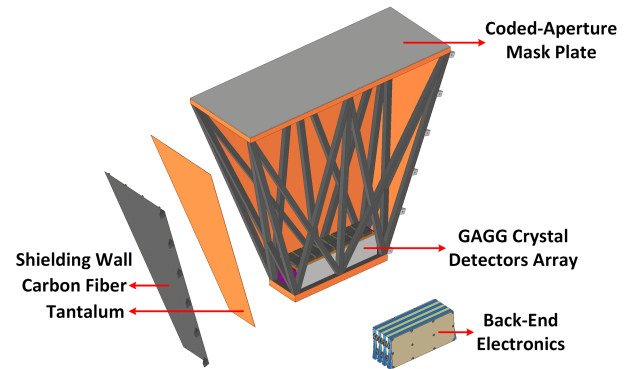


Figure 15 Schematic drawing of W2C. W2C consists of four main parts: coded-aperture mask plate, GAGG detectors array, shielding walls and back-end electronics.

of hot spots based on coding characteristics. Because the mask blocking and detector interaction depths are both energy dependent, depth correction is also applied to both the coded mask and the detectors to improve localization accuracy, using the accurate energy spectrum of the detected gamma-ray burst spectral features to improve localization accuracy.

- ASIC-controlled silicon photo-multiplier (SiPM) readout. It employs high-light-output Gadolinium Aluminum Gallium Garnet doped with Cerium (GAGG) crystal arrays coupled with high quantum efficiency SiPM arrays, optimized for balanced detection efficiency in medium-high-energy gamma rays and low-energy X-ray fluorescence. It also features ASIC-based pixel-by-pixel readout of SiPM arrays with low electronic noise, ensuring 10-1000 keV energy coverage. The readout electronics system originates from the POLAR-2 project [41].

The coded-aperture mask plate of W2C is primarily composed of three layers of materials: the top layer is a 1.5 mm thick carbon fiber, the middle layer consists of randomly distributed 1 mm thick tungsten alloy block pieces, and the bottom layer is another 2.5 mm thick carbon fiber material. The upper and lower layers of carbon fiber have randomly placed

apertures with an open area ratio of 50%. X-rays passing through apertures within the W2C field of view will generate hits on the detector, while X-rays blocked by tungsten alloy blocks in the middle layer within a certain energy range (≤ 100 keV) will not be detected. Note that the mask does not block X-ray photons above 100 keV effectively, in order to minimize the weight of the mask and maximize the spectral measurement capability to transients at energies above 100 keV. The size of the tungsten alloy blocks and the apertures matches the GAGG pixel size, both being $5.75 \text{ mm} \times 5.75 \text{ mm}$. The design of the W2C coded-aperture mask plate is shown in Figure 16.

In addition to the coded-aperture mask plate at the top, the W2C payload is surrounded by shielding walls on all sides to block most of the X-ray photons and low-energy charged particles in orbit, thereby ensuring the sensitivity and imaging localization accuracy. As shown in Figure 15, the wall of shielding in W2C consists mainly of two layers: the outer layer is made of 1 mm thick carbon fiber material, providing structural support, and the inner layer is made of 1 mm thick tantalum, serving as the primary shielding material.

The W2C GAGG scintillator detector array consists of a total of 16 detector units organized in a 2×8 array. This configuration is primarily designed to accommodate the spatial constraints of the satellite platform. Each detector unit is composed of 64 GAGG scintillator crystal pixels in an 8×8 array. The dimension of each pixel is $5.75 \text{ mm} \times 5.75 \text{ mm} \times 20 \text{ mm}$, and Enhanced Specular Reflector (ESR) reflective film is used between the pixels to reflect and isolate the fluorescent signals generated within the crystals. The pitch between adjacent pixels is 6.25 mm. The GAGG crystal array module is inserted in a carbon fiber socket for mechanical support and installation purposes. The signals generated within the GAGG crystals are collected and read out by the SiPM array board of the front-end electronics. The SiPM array board consists mainly of 64 small pieces of SiPMs from Hamamatsu, with each SiPM corresponding to the signal readout of one GAGG pixel. In addition to the SiPM board, the front-end electronics also includes an ASIC board and an interface board. The ASIC board contains key electronic components, such as the ADC and FPGA for reading out the signals from the SiPMs, while the interface board is used for communication with the back-end electronics. A schematic diagram of the W2C GAGG crystal detector array is shown in Figure 17.

The back-end electronics system of W2C is primarily used for payload triggering and the implementation of imaging algorithms, as well as transmitting payload data to the satellite platform, providing control commands, and managing power supply for the payload. Its main functions include:

- Communicating with the 16 detector units to read the

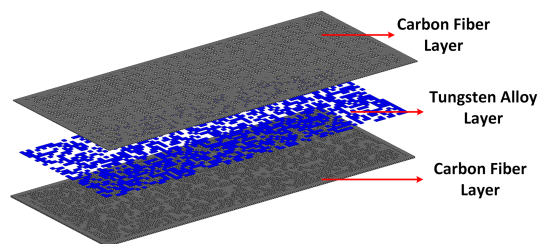


Figure 16 Design of the the coded-aperture mask plate of W2C.

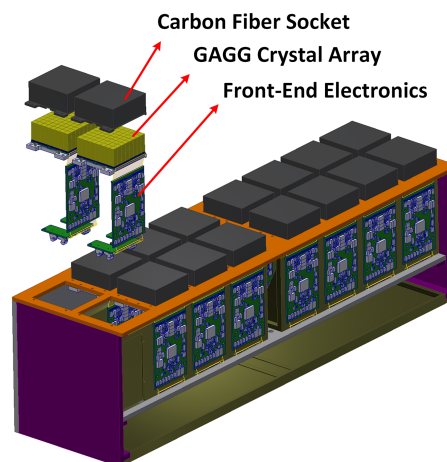


Figure 17 Schematic diagram of the GAGG crystal detector array of W2C.

physical event data packets.

- Managing science data, implementing trigger and localization functions, and forming event-by-event data packets.
- Performing remote control, telemetry, and status configuration for the detector units.
- Interfacing with the platform to process data, complete trigger, localize, and send science data packets.
- Interfacing with the platform computer for remote control and telemetry, completing the sending and receiving of remote control and telemetry data packets.
- Receiving the PPS signal from the platform computer to achieve system time synchronization.
- Implementing temperature telemetry and heater power supply functions for the temperature control module.
- Managing the primary power distribution for the system.
- Switching the system's operational modes.

Using a prototype of the GAGG scintillator detector unit (with GAGG crystal pixel dimensions of $5.75 \text{ mm} \times 5.75 \text{ mm} \times 5 \text{ mm}$), preliminary performance tests were conducted with a hard X-ray beam. Figure 18 shows the spectrum measured with this detector unit obtained using a 60 keV hard X-ray beam. In addition to the 60 keV beam energy peak in the spectrum, there is also an escape peak of approximately

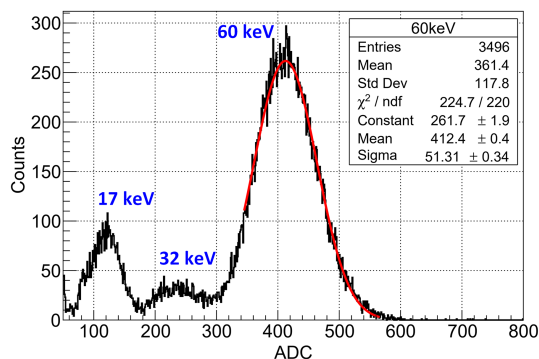


Figure 18 Measured spectrum of the GAGG scintillator detector unit prototype with a hard X-ray beam. Black curve: measured data. Red curve: fitted with Gaussian function. The beam energy is 60 keV. Three peaks are visible in the spectrum: the 60 keV peak, the 32 keV fluorescence from Barium due to the BaSO_4 housing, and the 17 keV escape peak.

17 keV due to the K_α characteristic X-ray energy of Gadolinium (Gd) in GAGG, which is about 43 keV. Furthermore, since barium sulfate (BaSO_4) was used as the reflective layer material between the GAGG crystal pixels in this detector unit prototype, the measured spectrum also includes a barium fluorescence line that corresponds to about 32 keV.

The large FoV of W2C provides unique opportunities to detect ~ 15 GRBs per year. The burst alert system is modelled following the design of the SVOM mission [42] and elements of the INTEGRAL BAS [43].

Two onboard trigger algorithms are foreseen: an image trigger, which performs systematic image deconvolution on long time scales, and a count rate trigger, which, as a first step, selects short time scales of counts in excess over background to be deconvolved in a second step. The detection of an uncatalogued source gives rise to a localized burst candidate.

However, W2C has not yet been adopted as a primary eXTP payload, due to some programmatic issues; it will likely be approved in a later stage and eventually installed onboard the eXTP platform as a secondary instrument. Currently, the required weight, power, and interfaces have been reserved in the design of the satellite platform. It is also possible to double the scale of W2C and mount it on the top surface of the platform (its FoV is co-aligned with that of SFA and PFA), if a different and more powerful launcher is used to replace the current baseline launcher CZ-3B G5 described in sect. 4.2.

4 The mission profile

4.1 Satellite system

The eXTP satellite stowed during launch is shown in Figure 19. Figure 20 is a picture of the main structure of the

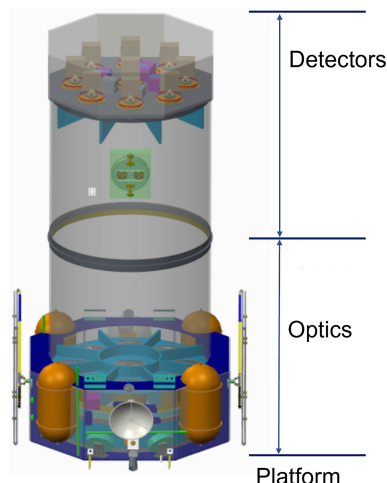


Figure 19 The eXTP satellite stowed during launch (diameter 3755 mm \times 6604 mm).

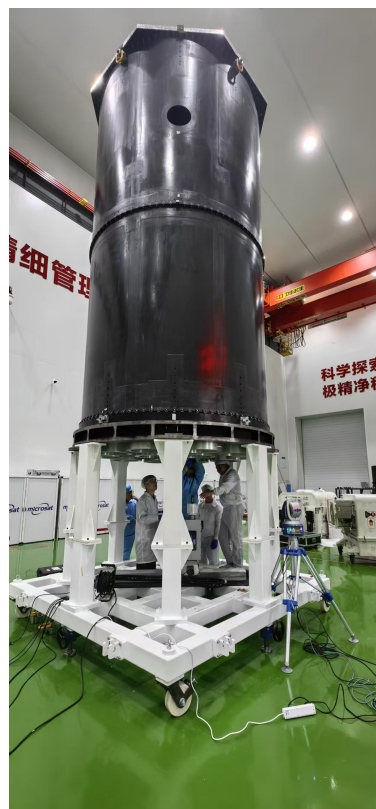


Figure 20 The main structure of the eXTP satellite, in which the mirrors and focal plane cameras are accommodated. Note that the structural models of mirrors (just above the engineers) and cameras (at the top) were installed for mechanical vibration tests. The tests results show that the mirrors and cameras were still well aligned within the requirements after vibrations.

eXTP satellite, in which the mirrors and focal plane cameras are accommodated. The deployed configuration is shown in Figure 21.

The main specifications of the satellite system are

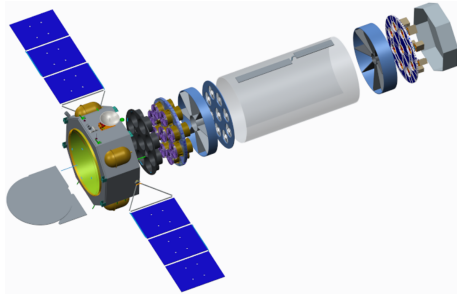


Figure 21 The expanded view of the deployed satellite is shown. In orbit the eXTP encumbrance is 4255 mm × 8800.9 mm × 12958.3 mm.

as follows:

- Orbit altitude: apogee: ≥ 100000 km, perigee: ~ 5000 km.
- Orbit type: high elliptical orbit.
- Orbit inclination: $\sim 28.5^\circ$.
- Total satellite mas: ≤ 3970 kg.
- Focusing mirror pointing (3σ): $\leq 1.1'$ (SFA&PFA, deviation of each focusing mirror's optical axis relative to celestial target).
- Focal plane detector position (3σ): axial ≤ 1 mm, radial ≤ 0.5 mm (relative to focusing mirror's focal point).
- Pointing method: three-axis stabilized inertial pointing.
- Pointing accuracy: $\leq 3''$ (3σ).
- Attitude stability: $\leq 2''/s$ (3σ).
- Attitude measurement accuracy: $\leq 1''$ (3σ) (star sensor).
- Micro-vibration: $\leq 1.2''$ (rms, 10-2000 Hz).
- Manoeuvring capability: 30° with stabilization in 10 min.
- Transmission band: Ku-band Earth communication.
- Data rate: 560/1120 Mbps (Ku).
- Storage capacity: supports 2-d scientific data storage.
- Control system: USB telemetry.
- Uplink rate: 2000 bps.
- Downlink rate: 16384/8192/4096/2048 bps.
- Particulate contamination: ≤ 1000 ppm (target: 300 ppm).
- Molecular contamination: focusing mirror $\leq 1 \times 10^{-7}$ g/cm², detector $\leq 1 \times 10^{-6}$ g/cm².
- Onboard time accuracy (GNSS available): ≤ 1 μ s.
- Processing speed: processor frequency ≥ 48 MHz.
- Design lifetime: 5-year nominal, additional 3-year extended.

4.2 Launch vehicle system

A CZ-3B G5 or equivalent launch vehicle will be used to launch the eXTP satellite into a 200×100000 km initial orbit. The technical requirements are as follows:

- Payload capacity: ≥ 3970 kg (excluding interface brackets, adapters, and transition cables).

- Satellite structural stiffness: lateral frequency (1st order): > 10 Hz; longitudinal frequency (1st order): > 30 Hz.
- Fairing requirements: net envelope: ≥ 3850 mm (transport with fairing from technical area to launch pad).
- Environmental conditions: temperature: 18-25°C; humidity: 30%-45%; cleanliness: class 10000.
- Thermal/pressure requirements: radiation heat flux ≤ 700 W m⁻² during ascent; free molecular heating ≤ 1135 W m⁻² during fairing separation; maximum pressure drop rate ≤ 6.9 kPa s⁻¹.
- Orbit insertion accuracy: semi-major axis deviation: ≤ 800 km; perigee altitude deviation: ≤ 41 km; inclination deviation: $\leq 0.22^\circ$; argument of perigee deviation: $\leq 0.71^\circ$ RAAN deviation: $\leq 1.09^\circ$.
- Separation requirements: attitude: +X axis earth-facing, +Y axis along velocity vector; relative velocity: ≥ 0.5 m/s; attitude angle error (3σ): $\leq 2^\circ$ (all axes); angular rate error (3σ): $\leq 0.5\%$ s⁻¹ (all axes).

4.3 Launch site system

The launch site system is responsible for rocket/satellite testing, launch operations, and facility management. The technical requirements are as follows:

- Test complex. Environment: class 100000 cleanliness, 18-25°C, 30%-45% RH; nitrogen supply: support for satellite's high-purity nitrogen system.
- Launch area. Fairing environment: class 10000 cleanliness, (20±3)°C, 30%-50% RH; nitrogen interface: dedicated purge system on launch tower.

4.4 Tracking & control system

The technical specifications for the tracking & control system are as follows:

- USB system: uplink rate: 2000 bps (BER $\leq 1 \times 10^{-6}$); downlink rate: 16384 bps (BER $\leq 1 \times 10^{-5}$).
- Initial tracking: ≥ 110 s contact at 5° elevation (TBC).
- Routine operations: ≥ 4 daily contacts (≥ 30 min total); CCSDS-compliant telemetry/command formats.
- ToO response: routine ToO: ≤ 12 h implementation; priority ToO: next available contact; ≤ 2 ToO commands/day.
- Orbit determination (3σ): 1-orbit prediction error: ≤ 3.5 km; 2-orbit prediction error: ≤ 5 km; post-processed accuracy: 1-3 km position, ≤ 1 m/s velocity.
- Time calibration: correct when the clock drifts more than 500 ms (with 5 ms accuracy).

Here, ToO refers to external triggers received in ground. Autonomous pointing can be triggered by transients detected

with W2C onboard. On the other hand, if a LEO is eventually chosen, ToO responses to external triggers may also be very fast, similar to the EP and SVOM missions.

4.5 Ground support system

The primary tasks of the Ground Support System (GSS) are: (1) to organize and complete the planning and design of in-orbit operation schemes (including Ku-band data transmission station selection) based on scientific requirements and satellite payload operation modes; (2) complete the reception, recording, and ground transmission of downlinked data; (3) carry out scientific observation mission planning, schedule development, command generation (including Target of Opportunity (ToO) event handling), mission monitoring, and status analysis for comprehensive operations and management, ensuring in-orbit operation control of scientific missions; (4) process and analyse the quality of satellite downlinked data, produce edited-level products, and distribute them to the scientific application system; and (5) collect, archive, and manage scientific data products, provide long-term data release services, establish a scientific research support environment, and assist scientific users.

The key capabilities of the GSS are as follows:

- 5-year primary + 3-year extended mission support.
- Ku-band ground stations (QPSK modulation).
- ≤ 4 h routine/ ≤ 1 h emergency command generation.
- 10 min ToO command processing.
- Data processing within 1 h of acquisition.
- ≥ 6 PB archival storage capacity.

4.6 eXTP Science Data Center

The Science Data Center (SDC) is responsible for (1) soliciting and selecting observation proposals for the eXTP satellite, formulating scientific observation plans (including routine and ToO observation plans); (2) monitoring payload operations, conducting performance analysis, and coordinating investigations into anomalies; (3) developing eXTP quality models, performing ground-based simulations, establishing calibration databases using ground calibration results, and updating in-orbit calibration analyses and databases; (4) processing scientific observation data to generate advanced scientific data products and auxiliary data products; (5) developing eXTP data analysis software and providing technical support for data analysis; (6) designing mission-level end-to-end scientific simulation systems to produce end-to-end simulated scientific data; and (7) organizing research and application of scientific observation data; managing the release and storage of scientific data products and mission information during the mission operation phase. The eXTP data stor-

age and release, as well as service to the community, will be the sole responsibility of the National Space Science Center (NSSC) of CAS after the mission operation is terminated; actually NSSC will also store all eXTP data and can also release the data during the mission operation phase.

To achieve the scientific objectives of the eXTP quickly after satellite launch, the SDC must also conduct pre-research during the development phase, including completing theoretical models, simulations, development of specialized analysis tools, and development of a preliminary observation plan tuned to reach the scientific goals of the eXTP. This involves (1) in-depth studies of the fundamental properties and radiative characteristics of compact celestial objects, refining existing theoretical models and research methods, and simulating scientific objectives; (2) developing dedicated physical analysis tools based on multi-method observational results (light curves, energy spectra, images, modulation curves, etc.); and (3) formulating preliminary observation requirements and curating scientific observation source catalogue.

The requirements for the SDC are as follows:

- Mission planning for 5+3 year operations.
 - ToO response: ≤ 13 h implementation for routine ToO; ≤ 20 min planning for priority ToO.
 - Payload monitoring: ≤ 5 s anomaly alert.
 - Data processing: ≤ 8 h calibration product generation
- End-to-end simulation system.
- Products: ≥ 5 PB data storage; white papers.

5 Observing strategy

The primary objective of the observation strategy is to ensure the best possible scientific outcome for the mission, opening the mission to the scientific community, while ensuring a return to the institutions and countries that financially supported the mission. Therefore, it is foreseen that eXTP will operate as an observatory open to the scientific community. Observation time will be allocated through annual announcement of opportunities and through scientific peer review. A fraction of the observing time will be allocated to key core projects that should ensure that the core science goals of the mission are reached. The mission will be designed to react fast to transient events, e.g., outbursts, performing flexible ToOs. ToOs (outside the state changes of sources defined in the guest observer program and in the key projects) can be proposed by the scientific community, and the Principal Investigator (PI) of eXTP will decide whether to schedule the proposed observation, after consulting the relevant key members of the eXTP team. Depending on the nature of the ToO, either the one-year proprietary data rule can be applied, or the data will be made available to the science community

in general. Standard one-year proprietary data rights are assumed for the pointed instruments, and after this period, all data shall become public. For the W2C, no proprietary data rights will apply, and these data should be made available to the community on a much shorter time scale. During routine operations, several pre-product data will be produced typically in 3 h after the observation. The data of the Burst Alert System will be distributed to the community as soon as possible using the appropriate systems, and no data rights will be applied.

6 Conclusions

In this paper, we have presented the main scientific goals, technical and technological aspects of the scientific payload of the eXTP mission, the performance of the instruments, and the main aspects of the mission. The eXTP mission is designed to address key questions of physics in the extreme conditions of ultra-dense matter, strong field gravity, and the strongest magnetic field existing in nature. The payload includes two narrow field instruments: the SFA, characterized by a large area at soft energies, and the PFA, an X-ray polarimeter whose effective area is about five times that of the polarimeter onboard the IXPE mission [21]. The science payload is completed by wide-field monitoring capabilities. This combination will enable, for the first time ever spectral-timing-polarimetry studies of a large number of objects populating the time variable Universe. In addition to investigating fundamental physics, eXTP will play a major role in the time-domain and multi-messenger era and become a very powerful observatory for astrophysics, providing data on a variety of galactic and extragalactic objects. In particular, the W2C will be able to detect the electro-magnetic counterparts of transient sources of the multi-messenger Universe, including gravitational wave sources and cosmic neutrinos sources.

The mission is led by China and is executed under the management of the CAS National Space Science Center, within the framework of the activities of the CAS Bureau of Major R&D Programs. IHEP of CAS leads the science consortium and is responsible for coordinating all science payload contributions within China and from international partner countries and agencies.

The Chinese team acknowledges the support of the National Natural Science Foundation of China (Grant No. 12333007), the International Partnership Program of Chinese Academy of Sciences (Grant No. 113111KYSB20190020), and the Strategic Priority Research Program of the Chinese Academy of Sciences (Grant No. XDA15020100). The Italian collaboration acknowledges support by ASI, under the dedicated eXTP agreements and agreement ASI-INAF n.2017-14-H.O., by INAF and INFN under project REDSOX. The German team acknowledges support from the Deutsche Zentrum für Luft- und Raumfahrt, the German Aerospace Cen-

ter (DLR). The Spanish authors acknowledge support from MINECO grant ESP2017-82674-R and FEDER funds.

Conflict of interest The authors declare that they have no conflict of interest.

- 1 S. N. Zhang, M. Feroci, A. Santangelo, Y. W. Dong, H. Feng, F. J. Lu, K. Nandra, Z. S. Wang, S. Zhang, E. Bozzo, et al., *Proc. SPIE*, **9905**, 99051Q (2016).
- 2 S. N. Zhang, A. Santangelo, M. Feroci, Y. P. Xu, F. J. Lu, Y. Chen, H. Feng, S. Zhang, S. Brandt, M. Hernanz, et al., *Sci. China-Phys. Mech. Astron.* **62**, 029502 (2019).
- 3 A. Santangelo, S. N. Zhang, M. Feroci, M. Hernanz, F. LU, and Y. Xu, in *Handbook of X-ray and Gamma-ray Astrophysics*, edited by C. Bambi, and A. Santangelo (Springer, Singapore, 2024), p. 1201-1229.
- 4 A. Li, A. L. Watts, G. Zhang, S. Guillot, Y. Xu, A. Santangelo, S. Zane, H. Feng, S.-N. Zhang, M. Ge, et al., *Sci. China-Phys. Mech. Astron.* **68**, 119503 (2025).
- 5 Q. Bu, C. Bambi, L. Gou, Y. Xu, P. Uttley, A. De Rosa, A. Santangelo, S. Zane, H. Feng, S.-N. Zhang, et al., *Sci. China-Phys. Mech. Astron.* **68**, 119504 (2025).
- 6 M. Ge, L. Ji, R. Taverna, S. Tsygankov, Y. Xu, A. Santangelo, S. Zane, S.-N. Zhang, H. Feng, W. Chen, et al., *Sci. China-Phys. Mech. Astron.* **68**, 119505 (2025).
- 7 S.-X. Yi, W. Zhao, R.-X. Xu, X.-F. Wu, G. Stratta, S. Dall’Osso, Y.-J. Xu, A. Santangelo, S. Zane, S.-N. Zhang, et al., *Sci. China-Phys. Mech. Astron.* **68**, 119506 (2025).
- 8 P. Zhou, J. Mao, L. Zhang, A. Patruno, E. Bozzo, Y. Xu, A. Santangelo, S. Zane, S.-N. Zhang, H. Feng, et al., arXiv: *Sci. China-Phys. Mech. Astron.* **68**, 119507 (2025).
- 9 A. L. Watts, W. F. Yu, J. Poutanen, S. Zhang, S. Bhattacharyya, S. Bogdanov, L. Ji, A. Patruno, T. E. Riley, P. Bakala, et al., *Sci. China-Phys. Mech. Astron.* **62**, 029503 (2019).
- 10 A. Santangelo, S. Zane, H. Feng, R. X. Xu, V. Doroshenko, E. Bozzo, I. Caiazzo, F. C. Zelati, P. Esposito, D. González-Caniulef, et al., *Sci. China-Phys. Mech. Astron.* **62**, 029505 (2019).
- 11 A. D. Rosa, P. Uttley, L. J. Gou, Y. Liu, C. Bambi, D. Barret, T. Belloni, E. Berti, S. Bianchi, I. Caiazzo, et al., *Sci. China-Phys. Mech. Astron.* **62**, 029504 (2019).
- 12 J. J. M. in’t Zand, E. Bozzo, J. L. Qu, X. D. Li, L. Amati, Y. Chen, I. Donnarumma, V. Doroshenko, S. A. Drake, M. Hernanz, et al., *Sci. China-Phys. Mech. Astron.* **62**, 029506 (2019).
- 13 Y. Dong, *Proc. SPIE*, **9144**, 91443O (2014).
- 14 M. Feroci, L. Stella, M. van der Klis, T. J. L. Courvoisier, M. Hernanz, R. Hudec, A. Santangelo, D. Walton, A. Zdziarski, D. Barret, et al., *Exp. Astron.* **34**, 415 (2012).
- 15 M. Feroci, J. W. den Herder, E. Bozzo, D. Barret, S. Brandt, M. Hernanz, M. van der Klis, M. Pohl, A. Santangelo, L. Stella, et al., *Proc. SPIE*, **9144**, 91442T-1, (2014).
- 16 H. Rauer, C. Catala, C. Aerts, T. Appourchaux, W. Benz, A. Brandeker, J. Christensen-Dalsgaard, M. Deleuil, L. Gizon, M. J. Goupil, et al., *Exp. Astron.* **38**, 249 (2014).
- 17 K. Jahoda, J. H. Swank, A. B. Giles, M. J. Stark, T. Strohmayer, W. W. Zhang, and E.H. Morgan, *Proc. SPIE*, **2808**, 59 (1996).
- 18 M. C. Weisskopf, B. Brinkman, C. Canizares, G. Garmire, S. Murray, and L. P. van Speybroeck, *Publ. Astron. Soc. Pac.* **114**, 1 (2002).
- 19 D. de Chabure, R. Lainé, K. van Katwijk, and P. Kletzkine, *ESA Bull.* **100**, 30 (1999).
- 20 K. C. Gendreau, Z. Arzoumanian, and J. K. Adkins, *J. Astron. Telesc. Instrum. Syst.* **3**, 021008 (2017).
- 21 M. C. Weisskopf, P. Soffitta, L. Baldini, B. D. Ramsey, S. L. O’Dell, R. W. Romani, G. Matt, W. D. Deinger, W. H. Baumgartner, R. Bellazzini, et al., *J. Astron. Telesc. Instrum. Syst.* **8**, 026002 (2022).
- 22 W. M. Yuan, C. Zhang, Y. Chen, S. L. Sun, Y. H. Zhang, W. Cui, Z. X. Ling, M. H. Huang, D. H. Zhao, W. X. Wang, et al., *Sci. Sin.-Phys. Mech. Astron.* **48**, 039502 (2018).

- 23 European Space Agency (ESA), *NewAthena Factsheet: Mission Summary* (European Space Agency, Paris, 2025).
- 24 P. Predehl, R. Andritschke, W. Becker, W. Bornemann, H. Bräuninger, H. Brunner, T. Boller, V. Burwitz, W. Burkert, N. Clerc, et al., *Proc. SPIE*, **9144**, 91441T, (2014).
- 25 O. Citterio, G. Conti, E. Mattaini, E. Santambrogio, and B. Sacco, *Proc. SPIE*, **597**, 102 (1986).
- 26 D. N. Burrows, J. E. Hill, J. A. Nousek, J. A. Kennea, A. Wells, J. P. Osborne, A. F. Abbey, A. Beardmore, K. Mukerjee, A. D. T. Short, et al., *Space Sci. Rev.* **120**, 165 (2005).
- 27 M. Pavlinsky, A. Tkachenko, V. Levin, N. Alexandrovich, V. Arefiev, V. Babushkin, O. Batanov, Y. Bodnar, A. Bogomolov, A. Bubnov, et al., *Astron. Astrophys.* **650**, A42 (2021).
- 28 B. D. Ramsey, *Proc. SPIE*, **10399**, 1039907 (2017).
- 29 A. Altmann, T. F. Bechteler, R. Strecker, P. Lechner, R. Andritschke, G. Hauser, C. Fiorini, and K. Nandra, *Proc. SPIE*, **13093**, 130936Q (2024).
- 30 R. Bellazzini, G. Spandre, M. Minuti, L. Baldini, A. Brez, L. Latronico, N. Omodei, M. Razzano, M. M. Massai, M. Pesce-Rollins, et al., *Nucl. Instrum. Methods Phys. Res. Sect. A* **579**, 853 (2007).
- 31 R. Bellazzini, L. Baldini, A. Brez, E. Costa, L. Latronico, N. Omodei, P. Soffitta, and G. Spandre, *Nucl. Instrum. Methods Phys. Res. Sect. A* **510**, 176 (2003).
- 32 R. Bellazzini, A. Brez, E. Costa, M. Minuti, F. Muleri, M. Pinchera, A. Rubini, P. Soffitta, and G. Spandre, *Nucl. Instrum. Methods Phys. Res. Sect. A* **720**, 173 (2013).
- 33 E. Costa, P. Soffitta, R. Bellazzini, A. Brez, N. Lumb, and G. Spandre, *Nature* **411**, 662 (2001).
- 34 H. Feng, W. Jiang, M. Minuti, Q. Wu, A. Jung, D. Yang, S. Citraro, H. Nasimi, J. Yu, G. Jin, et al., *Exp. Astron.* **47**, 225 (2019).
- 35 H. Li, X. Long, H. Feng, Q. Wu, J. Huang, W. Jiang, M. Minuti, D. Yang, S. Citraro, H. Nasimi, et al., *Adv. Space Res.* **67**, 708 (2021).
- 36 P. Soffitta, L. Baldini, R. Bellazzini, E. Costa, L. Latronico, F. Muleri, E. Del Monte, S. Fabiani, M. Minuti, M. Pinchera, et al., *Astron. J.* **162**, 208 (2021).
- 37 R. Bellazzini, F. Angelini, L. Baldini, F. Bitti, A. Brez, M. Ceccanti, L. Latronico, M. Massai, M. Minuti, and N. Omodei, *Nucl. Instrum. Methods Phys. Res. Sect. A* **535**, 477 (2004).
- 38 R. Bellazzini, G. Spandre, M. Minuti, L. Baldini, A. Brez, F. Cavalca, L. Latronico, N. Omodei, M. M. Massai, C. Sgro', et al., *Nucl. Instrum. Methods Phys. Res. Sect. A* **566**, 552 (2006).
- 39 M. Minuti, L. Baldini, R. Bellazzini, A. Brez, M. Ceccanti, F. Krummenacher, L. Latronico, L. Lucchesi, A. Manfreda, L. Orsini, et al., *Nucl. Instrum. Methods Phys. Res. Sect. A* **1046**, 167674 (2023).
- 40 T. E. Strohmayer, and T. R. Kallman, *Astrophys. J.* **773**, 103 (2013).
- 41 M. Kole, N. De Angelis, N. Produit, F. Cadoux, Y. Favre, J. Greiner, J. Hulsman, S. Kusyk, H. Li, D. Rybka, et al., *Nucl. Instrum. Methods Phys. Res. Sect. A* **1080**, 170782 (2025).
- 42 J. L. Atteia, B. Cordier, and J. Wei, *Int. J. Mod. Phys. D* **31**, 2230008 (2022).
- 43 S. Mereghetti, D. Götz, J. Borkowski, R. Walter, and H. Pedersen, *Astron. Astrophys.* **411**, L291 (2003).